Available online at www.sciencedirect.com
SCIENCE DIRECT®
Journal of Catalysis 231 (2005) 159–171
JOURNAL OF CATALYSIS
www.elsevier.com/locate/jcat

Investigation of Ni-based alumina-supported catalysts for the oxidative dehydrogenation of ethane to ethylene: structural characterization and reactivity studies

E. Heracleous [a], A.F. Lee [b], K. Wilson [b], A.A. Lemonidou [a,*]

[a] *Department of Chemical Engineering, Aristotle University of Thessaloniki and Chemical Process Engineering Research Institute (CERTH/CPERI), PO Box 1517, University Campus, GR-54006 Thessaloniki, Greece*
[b] *Department of Chemistry, University of York, York YO10 5DD, UK*

Received 27 October 2004; revised 22 December 2004; accepted 13 January 2005

Abstract

In this study, we report the development of efficient Al_2O_3-supported Ni and promoted Ni–Me (Me = Mo, V, Nb, Ta, Co) catalysts for the oxidative dehydrogenation of ethane. The effect of nickel loading and the impact of the promoters on the performance of the materials are discussed in the light of a detailed physico-chemical characterization of the catalysts by N_2 adsorption, XRD, XPS, TGA-H_2, and UV-DRS. Nickel was found to interact strongly with alumina, forming surface nickel aluminate-like species in the submonolayer regime, whereas NiO crystallites formed on top of the nickel/alumina interface for multilayer coverages. XPS revealed a chemical modification of the NiO particles accommodated on the alumina support. In terms of catalytic performance, increasing the Ni loading was beneficial and boosted ethane conversion, which surpassed 40% at 450 °C for the highest nickel loading catalyst, whereas ethene selectivity was retained at high levels for all Ni/Al_2O_3 catalysts. Promotion with V, Mo, Co, Nb, and Ta significantly modified both structural and catalytic properties in ethane oxidative dehydrogenation. The introduction of niobium was the most beneficial for ethane ODH, increasing the reactivity toward ethane by more than 50% at the expense of a relatively small drop (10%) in ethene selectivity.

Keywords: Oxidative dehydrogenation; Ethane; Nickel catalysts; XPS

1. Introduction

Ethylene is a major building block of the petrochemical industry and is used in the production of diverse products ranging from solvents to plastics. Currently, ethylene is produced by steam cracking of various hydrocarbon feedstocks (ethane, LPG, naphtha, gas oils), a process that operates under severe conditions. In fact, the conversion of ethane to ethylene via steam cracking is the most energy-consuming step of the petrochemical industry, with energy requirements estimated around 26 GJ/ton ethylene produced. With the ethylene market growing at 2–3% per year [1] and fuel costs constantly rising, research efforts have been focused on the development of less energy-intensive processes for the production of ethylene.

Catalytic oxidative dehydrogenation of ethane is an attractive alternative route for the production of ethylene. Its major advantage, compared with the conventional method, is its high energy efficiency, since the process operates at low temperatures and involves an exothermic reaction, thus has considerably lower energy requirements. However, for a viable industrial application of this process, a highly active and selective catalytic system, able to efficiently transform ethane to ethylene and not to total oxidation products, CO_x, is necessary. Several catalytic systems have been proposed

* Corresponding author. Fax: +30 2310 996184.
E-mail address: alemonidou@cheng.auth.gr (A.A. Lemonidou).

0021-9517/$ – see front matter
doi:10.1016/j.jcat.2005.01.015

in the last decades as efficient for the ethane ODH reaction [2–9]. One of the best-performing catalysts has been reported since 1978 by Thorsteinson et al. [8] and consists of a mixture of Mo–V–Nb oxides operating at low temperature (< 400 °C) with relatively high efficiency. Ever since the pioneering work of Thorsteinson, a great variety of mixed metal oxides have been tested, with a great increase in recent years in the number of tested materials, by application of combinatorial methods [9]. Recently, Lopez Nieto and co-workers have developed a very promising catalytic formulation based on mixed Mo–V–Te–Nb oxides, exhibiting about 75% ethylene yields at low reaction temperature (350–400 °C). The enhanced catalytic activity of the proposed mixed oxides was related to the presence of a multifunctional $Te_2M_{20}O_{57}$ (M = Mo, V, Nb) orthorhombic phase [10].

Nickel catalysts constitute an important class of catalytic materials and are widely applied in many important reactions, such as hydrogenation [11], natural gas reforming for syngas production [12], dealkylation [13], etc. The good performance of nickel-containing materials in oxidative dehydrogenation was first reported by Schuurman et al. [14]. Alumina-supported nickel catalysts were tested in the oxidative dehydrogenation of ethane and exhibited very promising results [15,16], and multicomponent nickel-based materials for ethane ODH have recently been patented by Symyx Technologies [17,18]. The promotion of nickel with several metals has a great effect on the ability of the catalysts to both activate the ethane feed and selectively convert it to ethene. However, reports in literature dealing with the nature of the active sites in such materials in correlation with their performance in oxidative dehydrogenation are scarce.

In this study, we report the development of efficient Al_2O_3-supported Ni and promoted Ni–Me (Me = Mo, V, Nb, Ta, Co) catalysts for the oxidative dehydrogenation of ethane. The effect of nickel loading and the impact of the promoters on the performance of the materials are discussed in the light of a detailed characterization of the physicochemical properties of the catalysts by N_2 adsorption, XRD, XPS, TGA-H_2, and UV-DRS. These complementary methods provided valuable insight into the nature of the surface species on the supported catalysts.

2. Experimental

2.1. Catalyst preparation

Catalysts were prepared by conventional wet impregnation of the γ-Al_2O_3 support (Engelhard) with aqueous solutions of nickel nitrate, $Ni(NO_3)_2 \cdot 6H_2O$ (Fisher), except in the case of the Ni–Ta catalyst, where an ethanol solution of nickel acetate, $Ni(C_2H_3O_2)_2 \cdot 6H_2O$ (Fisher), was used. The promoted Al_2O_3-supported Ni–Me catalysts were prepared by simultaneous impregnation, with the use of NH_4VO_3 (J.T. Baker), $Co(NO_3)_2 \cdot 6H_2O$ (Merck), $(NH_4)_6Mo_7O_{24} \cdot 4H_2O$ (Fisher), ammonium niobium oxalate (Aldrich), and $(CH_3CH_2O)_5Ta$ (Aldrich) as precursor compounds for V, Co, Mo, Nb, and Ta, respectively. The Me/Ni atomic ratio was kept constant and equal to 0.176 in all samples. Mild heating of the aqueous solutions ensured full dissolution of the precursor salts. Before impregnation, the support was crushed and sieved to a particle size of 106–180 μm. After impregnation, the solvent was removed by evaporation under reduced pressure, and the resulting solid was dried overnight at 120 °C and calcined in synthetic air at 450 °C for 5 h. The unpromoted catalysts are referred to as xNiAl, where x indicates the weight percentage of Ni related to the weight of the catalyst, and the promoted samples are referred to as Ni–Me, where Me indicates the promoting metal (V, Co, Mo, Nb, and Ta). The total metal weight loading of the catalysts did not exceed 30 wt% in any sample.

Nickel aluminate ($NiAl_2O_4$), used as a reference compound, was prepared as described in the literature [19] by coprecipitation of a stoichiometric mixture of aluminum and nickel nitrate with 1 M NH_4OH solution to a final pH of 8. After filtering, washing, and drying, the precipitate was calcined in synthetic air at 900 °C for 11 h.

The NiO(II) reference compound was provided by Acros Organics and used without further treatment.

2.2. Catalyst characterization

Surface areas of the samples were determined by N_2 adsorption at 77 K, with the multipoint BET analysis method, with an Autosorb-1 Quantachrome flow apparatus. Before the measurements, the samples were dehydrated in vacuum at 250 °C overnight.

X-ray diffraction (XRD) patterns were obtained with a Siemens D500 diffractometer employing Cu-K_α radiation.

The reduction characteristics of the catalysts were studied by thermogravimetric analysis (TGA-H_2) on a Stanton-Redcroft STA750 thermobalance. Typically, 20–30 mg of the sample was loaded into an alumina crucible, and the temperature was raised from room temperature to 1100 °C at a heating rate of 20 °C/min, in a 10% H_2/He flow (20 cm^3/min). The system was maintained isothermally at 1100 °C for 15 min.

Diffuse reflectance UV–vis spectra (UV-DRS) were recorded in the 50,000–11,000 cm^{-1} range on a JASCO V-550 UV/vis spectrophotometer.

X-ray photoelectron spectroscopy (XPS) measurements were performed with a Kratos AXIS HSi instrument equipped with a charge neutralizer and a Mg-K_α X-ray source. Spectra were recorded at normal emission, with an analyzer pass energy of 20 eV and X-ray power of 225 W. Before spectral acquisition samples were outgassed overnight in the preparation chamber of the spectrometer. Each spectral region was signal-averaged for ∼ 20 scans to obtain a good signal-to-noise ratio. Peak fitting involved a Shirley background subtraction and subsequent deconvolution with the use of mixed Gaussian–Lorentzian functions.

Table 1
Nomenclature and physico-chemical characteristics of the catalysts

Catalyst	Ni loading (wt%)	Me loading (wt%)	Surface area (m^2/g)	NiO average crystal size (nm)	T_{max} of reduction (°C)
8NiAl	7.8	–	173.4	–	565
15NiAl	14.2	–	160.5	8.0	528
24NiAl	23.9	–	137	15.2	491
Ni–V	26	4	142.8	17.0	444
Ni–Mo	23.3	6.7	136.7	23.0	447
Ni–Co	25.5	4.5	130.1	20.0	300, 367, 490
Ni–Nb	23.5	6.5	156.9	26.5	334, 508
Ni–Ta	16.9	13	157.9	21.5	325

Fitting was performed with CASAXPS, Version 2.0.35, using the minimum number of peaks required to minimize the R-factor. Binding energies were referenced to C 1s of adventitious carbon at 285 eV.

2.3. Reactivity studies

The catalytic performance of the samples was measured in a fixed-bed quartz reactor. The catalyst particles were diluted with an equal amount of quartz particles of the same size to achieve isothermal operation. The temperature in the middle of the catalytic bed was measured with a coaxial thermocouple. The samples were activated in flowing oxygen at 450 °C for 30 min. The composition of the reaction mixture used was $C_2H_6/O_2/He = 7:7:63$.

The oxidative dehydrogenation of ethane was investigated in the temperature range from 300 to 500 °C. For the determination of the activity of the catalysts as a function of temperature, the weight of the sample was 0.7 g and the total flow was 77 cm^3/min. To obtain different ethane conversion levels at constant reaction temperature (400 °C), the W/F ratio was varied from 0.02 to 1.33 g s/cm^3. Complementary experiments investigating the reactivity of the catalysts toward the main product of interest, ethene, were also conducted. For the ethene oxidation experiments, the reaction conditions were kept identical to the ethane ODH experiments (T = 300–500 °C, 0.7 g catalyst, total flow 77 cm^3/min, reaction mixture composition $C_2H_4/O_2/He = 7:7:63$).

The reaction products were analyzed on-line with a Perkin–Elmer gas chromatograph equipped with a thermal conductivity detector (TCD). Two columns in a series-bypass configuration were used in the analysis: a Porapak Q and a MS 5A. The main reaction products were C_2H_4, CO_2, CO, and H_2O. Negligible amounts of oxygenates were observed at the reactor exit. The ethane/ethene conversion and the selectivity to the reaction products were calculated on a carbon basis. Closure of the carbon mass balance was better than ±1%.

The contribution of gas-phase initiated reactions was tested with experiments using an empty-volume reactor. The conversion of ethane/ethene at these experiments was lower than 1%, confirming that gas-phase reactions are negligible at the experimental conditions used for the activity tests.

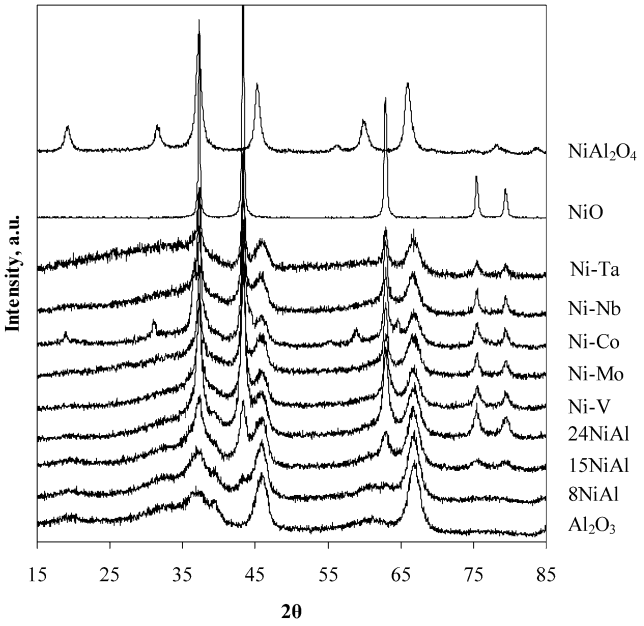

Fig. 1. X-ray diffraction patterns of the nickel-based catalysts and reference materials NiO, $NiAl_2O_4$ and Al_2O_3.

3. Results

3.1. Catalyst characterization

The composition and physico-chemical characteristics of the prepared catalysts are listed in Table 1. For the unpromoted catalysts, deposition of Ni on Al_2O_3 caused a gradual decrease in the specific surface area expressed per gram of catalyst, which drops from 184 m^2/g for pure calcined γ-Al_2O_3 to 137 m^2/g for the highest loading 24NiAl catalyst. However, the values of the surface area expressed per gram of support remain virtually unchanged, indicating that this apparent decrease is only a result of the fact that the deposited nickel does not contribute to the surface area. Promotion of the catalysts also did not cause significant variations in the surface area, except in the case of the Ni–Nb and Ni–Ta catalysts, where an increase was recorded. This latter observation was in line with expectations, since the Nb and Ta precursors have an organic nature and their decomposition during calcination should yield a more porous structure than for the inorganic nitrate precursor salts.

Investigation of the crystalline phases present in the catalysts was performed by X-ray diffraction (XRD) analysis. The resulting diffractograms appear in Fig. 1. All samples exhibited diffraction lines characteristic of the γ-Al_2O_3 support. For the 8NiAl catalyst, no Ni-containing phases were detected, indicating a well-dispersed, amorphous nickel structure on the surface of the support [20]. As the loading increases to 15 wt% Ni, diffraction lines at 2θ 43.3°,

63°, 75.5°, and 79.5° originating from bulk NiO begin to appear, becoming sharper and more intense in the 24NiAl sample, indicating larger nickel oxide particles with high crystallinity. Indeed, with the use of Scherrer's formula, average NiO particle sizes of 8 and 15 nm were found for the 15NiAl and 24NiAl catalysts, respectively. Bulk $NiAl_2O_4$ was not detected by XRD, as shown by the diffractogram of the pure phase that is included for comparison in Fig. 1.

The monolayer dispersion capacity of NiO on Al_2O_3 has been reported to range from 13 to 20 wt% Ni loading, as determined by ion scattering spectroscopy [21], XRD [22], and XPS [23]. The appearance of crystalline NiO in the 15NiAl sample indicates saturation of the alumina surface by two-dimensional Ni species and the genesis of multilayer/crystalline nickel phases.

The diffraction patterns of the promoted Ni–Me catalysts are also illustrated in Fig. 1. Again, only diffraction lines corresponding to crystalline NiO and Al_2O_3 were detected on the catalysts, except in the case of Ni–Co, where a small fraction of $CoAl_2O_4$ spinel phase was identified. Although $NiAl_2O_4$ and $CoAl_2O_4$ spinels give similar diffraction patterns, the lines at 2θ 59° and 65° in the diffractogram of the Ni–Co catalyst can be clearly assigned to cobalt aluminate, compared with the corresponding shifted lines of $NiAl_2O_4$ at 60° and 66°, respectively. However, the amount and size of the NiO crystallites (see Table 1) formed vary for the different promoters, even though the weight percentage of Ni loading remains essentially constant (with the exception of Ni–Ta catalyst). It seems that the introduction of promoting metals causes additional segregation of the nickel phase, with the largest effect induced by niobium, with NiO crystals of $\sim$ 26.5 nm.

Thermogravimetric analysis in the presence of a reductive atmosphere (TGA-H_2) was used to assess the reduction behavior of the prepared catalysts. The differential weight loss versus temperature allows the extraction of the reduction curves presented in Figs. 2A and 2B. The reduction profiles of the unsupported NiO and $NiAl_2O_4$ are also shown (Fig. 2A). Pure NiO exhibits a sharp reduction peak at 370 °C, whereas $NiAl_2O_4$ is much harder to reduce, exhibiting a broader peak with a maximum at 870 °C. For all unpromoted Ni/Al_2O_3 catalysts, a single broad reduction peak in the 490–560 °C range was recorded, with the T_{max} of reduction shifting to lower temperature with increasing Ni loading. These results confirm the strong metal–support interaction between nickel and alumina. The high temperature peak of the lowest loading 8NiAl catalyst could be attributed to surface nickel aluminate-like spinel species formed on the surface of the catalyst. The decrease in the reduction temperature maximum and the broad peaks recorded for the 15NiAl and 24NiAl catalysts are a result of contributions from strongly interacting surface nickel aluminate species and NiO crystallites (detected by XRD) accommodated on top of the nickel/alumina interface.

Many authors have postulated the existence of a "surface spinel" on the interface of Ni/Al_2O_3 catalysts. Lo Jacono et al. [24] proposed that this "surface spinel" accommodates nickel ions in octahedral and tetrahedral sites. According to Wu and Hercules [21], tetrahedrally coordinated nickel ions are hard to reduce, whereas octahedral nickel ions are readily reduced species, with the Ni_{tetr}/Ni_{oct} ratio decreasing with increasing loading. This rearrangement of nickel ions in octahedral sites with increasing loading could explain the shift in the temperature of reduction observed over the unpromoted catalysts.

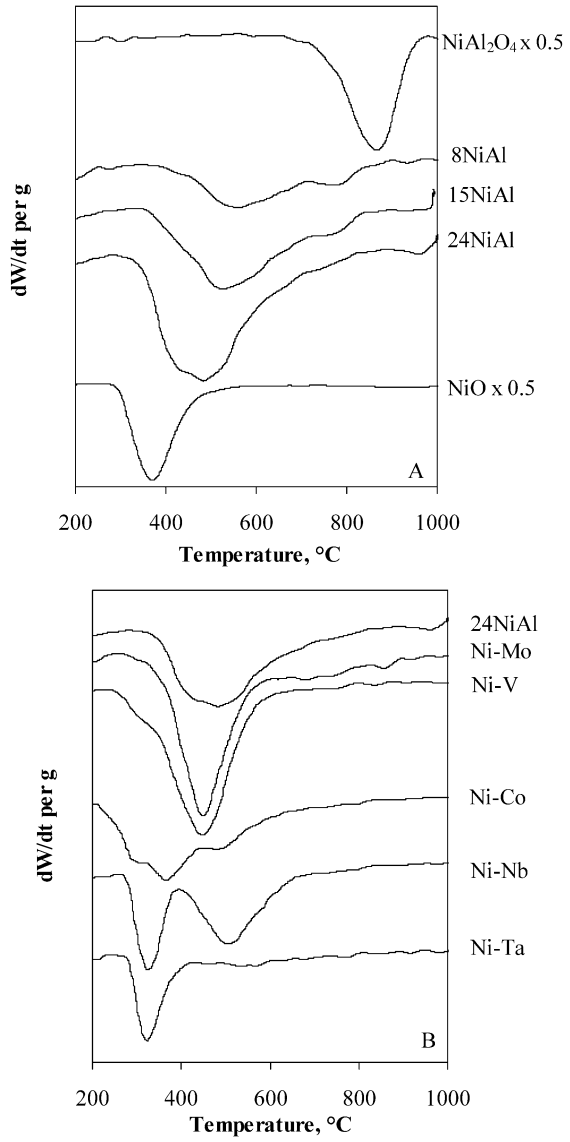

Fig. 2. Temperature-programmed reduction profiles obtained from H_2-TGA experiments. (A) Unpromoted Ni/Al_2O_3 catalysts and NiO, $NiAl_2O_4$ reference compounds; (B) metal promoted Ni/Al_2O_3 catalysts.

The introduction of the promoters induces significant changes in the reduction characteristics of the materials (Fig. 2B). Incorporation of the early transition metals V and Mo stimulates similar changes and shifts the temperature maximum at 445 °C, while the reduction profiles become narrower than in the case of the 24NiAl catalyst. The Ni–Co catalyst is reduced at an even lower temperature range; how-

ever, the peak is rather broad, with a maximum at 370 °C and shoulders at 300 and 490 °C. Cobalt, which is itself very reducible, seems also to significantly promote reduction of Ni species at lower temperature. The TPR profile of the Ni–Nb catalyst presents two distinct reduction peaks with maxima at 335 and 510 °C. Experiments performed with the Nb_2O_5 reference showed that the pure oxide remains essentially unreducible at temperatures up to 1100 °C, whereas studies on Nb_2O_5/Al_2O_3 catalysts report no hydrogen consumption for catalysts with loadings below 30 wt% Nb_2O_5 [25]. The two peaks in the Ni–Nb reduction profile are thus reasonably ascribed to two different distinct Ni species on the catalyst. Tantalum exhibits a reduction behavior similar to that of niobium, since neither pure Ta_2O_5 nor Ta_2O_5/Al_2O_3 can be reduced at the temperatures explored in this study [26]. Therefore, the single peak observed at 325 °C in the Ni–Ta spectrum is assigned to easily reducible modified Ni species on the surface of the catalyst.

Diffuse reflectance UV–vis spectroscopy was used to study the symmetry and coordination of the surface species of the catalysts under study. The reflectance spectra of unsupported NiO and pure $NiAl_2O_4$ phase, shown in Fig. 3, are first discussed. NiO has a rock salt structure with Ni ions in an octahedral coordination. The NiO spectrum is dominated by the NiO charge transfer band (CTB) at 19,600 cm^{-1} [27] and absorption bands in the 19,500–11,000 cm^{-1} range, due to the d–d transitions of octahedral Ni(II) in the NiO lattice. The band at 26,500 cm^{-1} and the strong band at 14,000 cm^{-1}, ascribed to the $^3A_{2g} \rightarrow {}^3T_{1g}(F)$ transition of octahedral Ni(II), are fingerprints for NiO [28]. The $NiAl_2O_4$ spectrum differs significantly from that of NiO; absorption bands at 18,000, 16,700–15,600 (doublet), and 14,000 cm^{-1} represent the $^3T_1 \rightarrow {}^1T_2$, $^3T_1 \rightarrow {}^3T_1(P)$ and $^3T_1 \rightarrow {}^1E$ transitions of tetrahedral Ni(II) ions in the Al_2O_3 lattice, and the band at 27,000 cm^{-1} is ascribed to

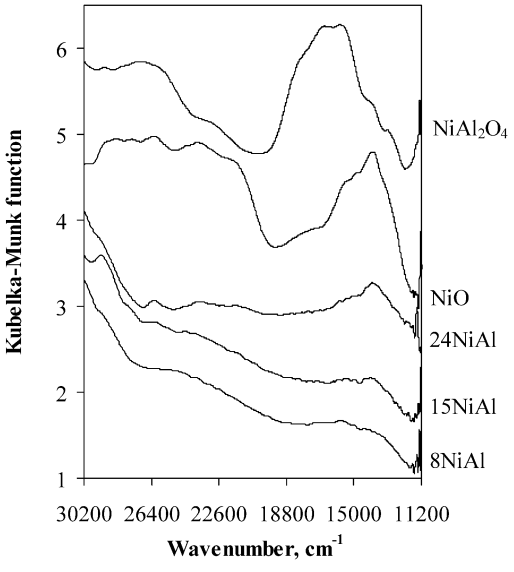

Fig. 3. Diffuse reflectance UV–vis spectra of the unpromoted Ni/Al_2O_3 catalysts and NiO, $NiAl_2O_4$ reference compounds.

the $^3A_{2g} \rightarrow {}^3T_{1g}(P)$ transition of octahedrally coordinated Ni ions [29]. Therefore, nickel aluminate can be described as a partial inverse spinel, which means that Ni(II) ions occupy both octahedral and tetrahedral sites of the oxygen lattice.

The spectra acquired for the 8NiAl, 15NiAl, and 24NiAl catalysts are presented together with the spectra of the reference compounds in Fig. 3. It should be mentioned that high absorbance was recorded over the whole measured wavelength range because of the dark (gray) color of the samples, indicating the presence of nickel in a nonstoichiometric form, which resulted in weak reflected bands. The spectrum of the 24NiAl closely resembles that of NiO with bands at 14,000 and 26,500 cm^{-1} indicating, in accordance with the XRD results, that the surface is mostly covered by NiO crystallites. The band at 14,000 cm^{-1}, indicating the presence of NiO crystals, is also present in the spectrum of the 15NiAl catalyst. However, in the spectra of both 8 and 15NiAl samples, contributions from Ni ions with tetrahedral coordination in the Al_2O_3 lattice are apparent from the band at 16,000 cm^{-1}. This confirms the formation of a "surface spinel" phase, as suggested by the TGA-H_2 data, even at calcination temperatures as low as 450 °C, and the migration of Ni ions from tetrahedral to octahedral coordination with increasing loading.

Because of the dark color and the high overall absorbance of the promoted nickel catalysts, no additional useful information could be extracted. Their spectra exhibited only strong NiO absorption bands, indicating the presence of nickel oxide crystallites on the surface of the materials.

X-ray photoelectron spectroscopy (XPS) was used to provide information about the oxidation state and the chemical environment of the elements present on the surface of the catalysts. Table 2 lists the binding energies (BEs) corresponding to the Ni $2p_{3/2}$, Ni $2p_{1/2}$, and O 1s levels for all the catalysts under study. Figs. 4 and 5 present the background subtracted Ni 2p and O 1s XP spectra obtained for the three unpromoted Ni/Al_2O_3 catalysts, together with those of pure NiO and nickel aluminate used as standards, and for the promoted catalysts, respectively. The values indicated in Table 2 and the included peaks shown in Figs. 4 and 5 arise from the deconvolution of the overall experimental peaks, according to the procedure described in the Section 2.

The Ni 2p spectrum of nickel oxide exhibits a clearly resolvable multiplet splitting of the $2p_{3/2}$ transition, with two states present at BEs of 853.4 and 855.1 eV, and a shake-up satellite at ∼ 860.5 eV, all characteristic of unsupported NiO [30,31]. The origin of this double structure in the Ni $2p_{3/2}$ core-level photoemission spectra of NiO remains a matter of controversy, and no unambiguous theoretical explanation of this phenomenon has yet been offered. Reports in the literature have correlated this extra high BE peak with changes in the ionic charge and coordination induced by nearby cation vacancies and thus indicate the presence of Ni^{3+} ions [32–34]. However, the enhancement of this extra peak upon sputtering of NiO single crystals [35], wherein the surface becomes oxygen deficient and the Ni valency is

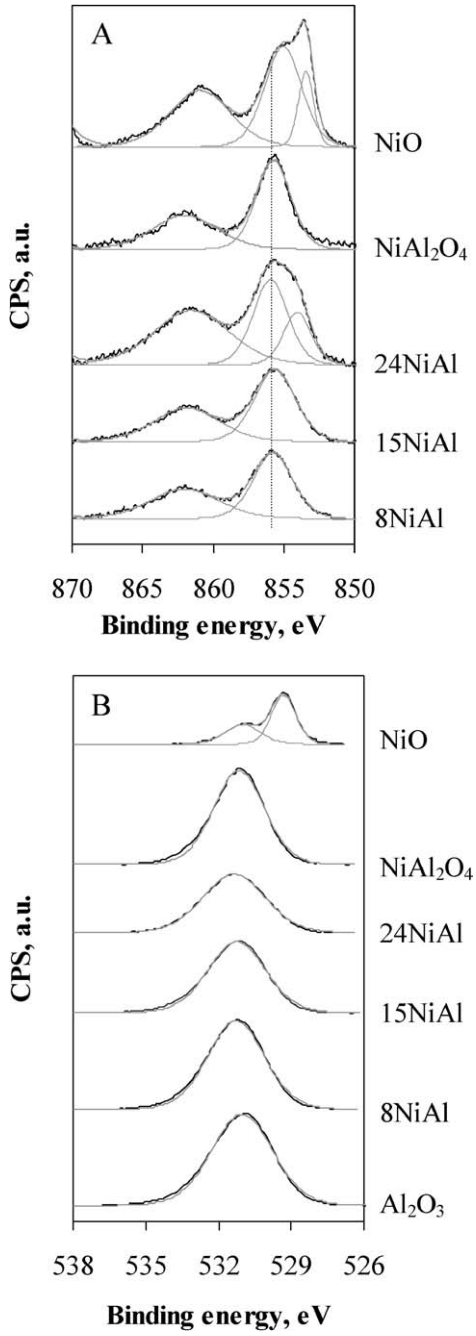

Fig. 4. X-ray photoelectron spectra of the unpromoted Ni/Al_2O_3 catalysts and NiO, $NiAl_2O_4$ reference compounds. (A) Ni 2p transition; (B) O 1s transition.

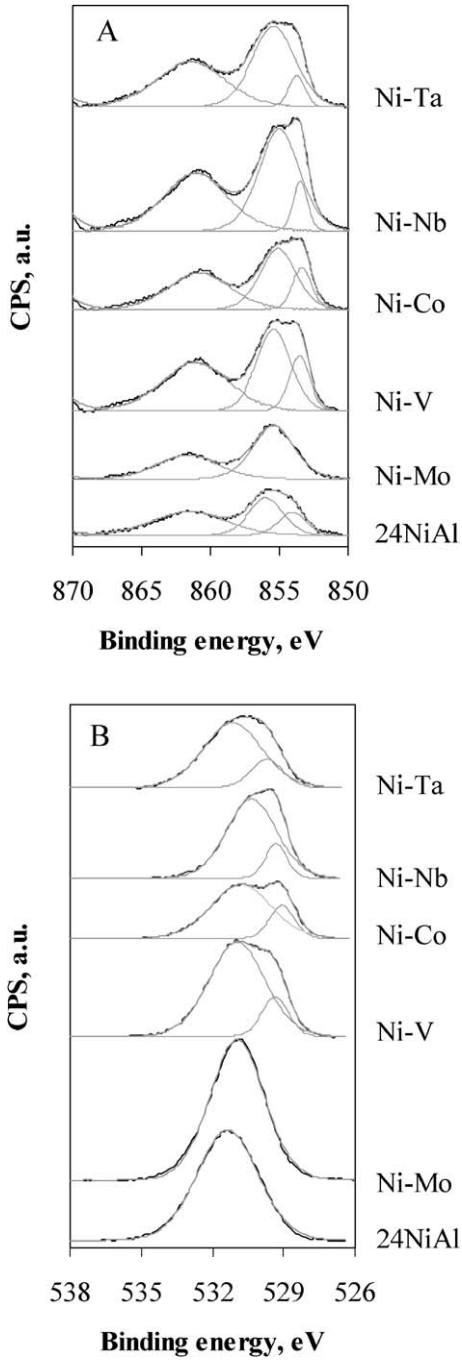

Fig. 5. X-ray photoelectron spectra of the metal promoted Ni/Al_2O_3 catalysts. (A) Ni 2p transition; (B) O 1s transition.

thus expected to decrease, renders this interpretation doubtful. Another interpretation offered by van Veenendaal and Sawatzky [36] suggests that this second peak is the result of a nonlocal screening mechanism, i.e., the result of a screening process by an electron that does not come from the oxygen atoms directly around the ionized Ni atom, but from neighboring NiO_6 units. If the double peak of the Ni $2p_{3/2}$ transition is explained by this non-local screening mechanism, then the appearance and intensity of this high BE feature will clearly be dependent on the structure arrangement and the nature and the valence of the surrounding atoms.

The O 1s spectrum for the NiO standard shows a main peak at 529.3 eV with contributions from a peak located at 531 eV. These can be ascribed to Ni–O and Ni–OH bonds [31], respectively, indicating substantial hydroxylation of the oxidic surface (37% contribution to the total oxygen content). It should be mentioned that the high BE component of the Ni $2p_{3/2}$ doublet cannot be assigned to Ni–OH species, since in situ heating of the sample caused the disappearance

Table 2
Binding energies of the Ni 2p and O 1s XP spectra

	Ni $2p_{3/2}$ BE (eV)	Ni $2p_{1/2}$ BE (eV)	O 1s BE (eV)
NiO	855.1 (77%) 853.4 (23%)	872	531 (37%) 529.3 (63%)
$NiAl_2O_4$	855.8	873.3	531.1
8NiAl	855.8	873.4	531.2
15NiAl	855.7	873.4	531.2
24NiAl	855.9 (67%) 854 (33%)	873.1	531.3
Ni–V	855.4 (71%) 853.5 (29%)	872.5	531 (83%) 529.4 (17%)
Ni–Mo	855.4	873.2	531
Ni–Co	854.9 (74%) 853.3 (26%)	872.1	531 (80%) 529.1 (20%)
Ni–Nb	855 (86%) 853.4 (14%)	872.3	530.3 (84%) 529.3 (16%)
Ni–Ta	855.4 (87%) 853.7 (13%)	872.8	531.1 (81%) 529.7 (19%)

of the 531 eV peak (hydroxyl groups), whereas the peak at 855.1 eV persisted.

Nickel aluminate is characterized by a Ni $2p_{3/2}$ binding energy of 855.8 eV with a spin-orbit splitting of 17.5 eV, in accordance with data from the literature [37]. The environment of nickel on the surface of the 8NiAl and 15NiAl catalysts is characteristic of Ni^{2+} ions present as highly dispersed surface nickel aluminate species, as shown by the binding energy of Ni $2p_{3/2}$ at 855.8 eV and the spin-orbit splitting value of 17.5 eV, which coincides with that of the $NiAl_2O_4$ standard but not with that of NiO, which is significantly larger (18.6 eV). As the nickel loading increases to 24 wt%, the Ni $2p_{3/2}$ peak becomes asymmetric, with a shoulder emerging at lower BE, concomitant with a decrease in the spin-orbit splitting. Best fitting is achieved with two peaks with maxima at 855.9 and 854 eV, indicating the presence of both nickel aluminate and NiO-like species on the surface. If we assume, based on our data, that monolayer saturation is achieved at $\sim$ 15 wt% Ni content, then the total Ni coverage on 24NiAl equals $\sim$ 1.6 ML. The relative contributions of the deconvoluted $NiAl_2O_4$ and NiO species (67 and 33%, respectively) support the notion that all of the surface nickel is strongly bound to the alumina support until completion of the monolayer. Above this threshold coverage, the excess nickel forms NiO particles atop the nickel–alumina interface. The BE of this surface nickel oxide species is upshifted compared with the reference bulk oxide, indicating either chemically modified NiO particles due to interaction with the alumina support or the nickel/alumina interface or reduced core-hole screening in the dispersed oxide thin film. This former observation nicely explains the absence of a low-temperature reduction peak, characteristic of bulk NiO, in the TPR pattern of 24NiAl, even though NiO was detected by XRD on the surface of the catalyst. It has been postulated that dispersed NiO loses its bulk electronic characteristics because of spin delocalization of 3d electrons toward the support, but retains the bulk crystallography, as indicated by XRD [38]. Concerning the O 1s XP spectra, no additional information can be extracted, since for the unpromoted alumina-supported nickel samples the major oxygen contribution is from the alumina itself, with a binding energy of 531.2 eV.

The introduction of metal promoters modifies the nickel environment at the alumina surface, as indicated by changes in Ni $2p_{3/2}$ and O 1s XP spectra presented in Figs. 5A and 5B, respectively. In the case of the Ni–Mo catalyst, the Ni 2p spectrum resembles that of the $NiAl_2O_4$ reference, consistent with a strong interaction between the surface nickel and the alumina support. There was no evidence for a nickel oxide component in the outermost surface of the catalyst, despite the observation of NiO crystallites by XRD for this Ni–Mo system. Together these suggest that such NiO particles may be encapsulated within a shell of nonstoichiometric nickel aluminate phase, rendering the oxide XPS invisible. The formation of a surface nickel molybdate, and thus the existence of strong interaction between Ni and Mo, can be excluded, since the spin-orbit splitting of $NiMoO_4$ has been reported as 18.6 eV [39], significantly higher than that measured for our catalyst (17.8 eV). Molybdenum is present on the surface as Mo^{6+}, as indicated by the Mo $3d_{5/2}$ and Mo $3d_{3/2}$ peak positions at 232.7 and 235.8 eV (not shown). The slight shift to lower BE (0.5 eV) and accompanying Mo 3d peak broadening relative to that of a measured MoO_3 reference (FWHM = 2 eV for Ni–Mo versus 1.3 eV for MoO_3) may reflect the influence of the underlying alumina support [40].

The nickel surface environment is strongly perturbed by the presence of vanadium. The Ni $2p_{3/2}$ spectrum exhibits the doublet structure typical of the oxide, with peaks at 855.4 and 853.5 eV BE. Vanadium appears to hinder the strong interaction between nickel and alumina seen for the 24NiAl and Mo-promoted samples, thus favoring enhanced nickel oxide formation. The peak at 855.4 eV is at slightly higher BE than that of bulk NiO and may contain contributions from $NiAl_2O_4$-like species still present on the surface, or reflect particle-size effects and non-local screening mechanisms as discussed previously. The enhanced NiO formation is also confirmed by the O 1s XP spectrum, which can be deconvoluted into two states, attributed to Ni–O and Al–O bonds at 529.4 and 531 eV, respectively. The V $2p_{3/2}$ transition occurs at 516.7 eV, and comparison with values for reference V^{5+} compounds (517.2–517.6 eV) [41] suggests that vanadium in the Ni–V catalyst is stabilized in a partially reduced V^{4+} state [42].

Tantalum incorporation led to similar changes in the shapes of Ni 2p and O 1s spectra, suggesting a similar weakening of the nickel–alumina interaction, resulting in (albeit less pronounced) NiO formation. Tantalum, in turn, appears to exist in its surface oxidic form as Ta^{5+} species, indicated by a characteristic Ta 3d doublet at 231 and 242.4 eV [43].

There was no evidence for nickel aluminate-like species in the XPS spectra of the Ni–Nb and Ni–Co catalysts, with the Ni 2p and O 1s lineshapes and BE identical to those of pure bulk NiO. It seems that in the presence of these two promoters, the interaction between nickel and alumina is much weaker than for all the other samples. There was also no evidence for any interaction between nickel and either niobium or cobalt. The Nb 3d spectrum contained a doublet at BEs of 207.5 eV ($3d_{5/2}$) and 210.3 eV, indicative of Nb^{5+} in the oxidic form [44]. Cobalt, on the other hand, appears to be stabilized on the surface as Co^{2+}, with Co $2p_{3/2}$ and $2p_{1/2}$ peaks at 780.2 and 795.6 eV. Although Co^{2+} and Co^{3+} give very similar Co 2p XP features, Co^{2+} high-spin compounds are characterized by an intense shake-up satellite structure at ca. 786 and 803 eV, which is weak or missing in the low-spin Co^{3+} compounds [45]. This satellite structure was indeed present in the Co 2p spectrum of Ni–Co at 785.7 and 802.4 eV, allowing the unequivocal assignment of the Co +2 oxidation state on the catalyst surface.

The contribution of the ∼ 855 eV peak in the nickel spectrum, which may arise from screening electrons from neighboring NiO_x units, is lower in Ni–Nb and higher in Ni–Co compared with the reference NiO (see Table 3). As mentioned above, the appearance and intensity of this high BE satellite depend strongly on the local structure around Ni surface atoms. Although XPS only identified the presence of NiO on the Ni–Nb catalyst, the corresponding reduction profile suggests the presence of two kinds of reducible nickel species. Based on the temperature of these two reduction processes, they may be attributed to Ni–O–Ni and Ni–O–Nb bonds, although it is not possible to discount the role of particle size effects and defects within a pure NiO surface phase arising indirectly from the coadsorbed Nb.

In addition to the nature and oxidation state of supported metal species, XPS also offers valuable information regarding the surface composition of these bimetallic catalysts. The values of the nominal and surface (determined by XPS using the appropriate sensitivity correction factors) Ni/Al and Me/Ni (where Me = V, Co, Mo, Nb, and Ta) atomic ratios are listed in Table 3, with the use of the appropriate sensitivity correction factors. The surface Ni/Al atomic ratios are generally higher than the corresponding nominal ones, indicating a nickel-enriched surface. This is not surprising, given that the materials were prepared by impregnation of the alumina support, wherein the active Ni phase is dispersed across the surface. In the series of the unpromoted Ni/Al_2O_3 catalysts, increasing the total Ni loading gave a nonlinear rise in the surface Ni content, with a more pronounced increase for the highest loading 24NiAl catalyst. This observation is consistent with the previous characterization results, which show that Ni loadings greater than 15 wt% saturate the alumina monolayer, inducing a switchover from $NiAl_2O_4$ growth (exposing significant surface Al) to a crystalline NiO capping overlayer. This attenuates the underlying $NiAl_2O_4$ interface and alumina support, significantly increasing the Ni/Al surface ratio.

Table 3
Nominal and surface Ni/Al and Me/Ni (Me = V, Mo, Co, Nb, Ta) atomic ratios determined by XPS

	Nominal atomic ratio		Surface atomic ratio	
	Ni/Al	Me/Ni	Ni/Al	Me/Ni
8NiAl	0.073	–	0.241	–
15NiAl	0.143	–	0.319	–
24NiAl	0.273	–	0.710	–
Ni–V	0.323	0.176	1.620	0.189
Ni–Mo	0.289	0.176	0.684	0.279
Ni–Co	0.316	0.176	1.929	0.105
Ni–Nb	0.291	0.176	4.216	0.131
Ni–Ta	0.227	0.176	2.317	0.112

The surface Ni content of the Me-promoted nickel catalysts provides interesting comparisons. Note that the nominal Ni/Al ratios were very similar for the 24NiAl catalyst and all of the promoted samples, with the exception of the Ni–Ta catalyst. However, the surface Ni/Al atomic ratio exhibits large variance between samples. In general, the presence of the promoting metals results in a significant enrichment of the surface nickel in comparison with the unpromoted 24NiAl catalyst (from ∼ 2 to 6 times higher). Ni–Mo was the only exception, in which the surface was impoverished in nickel and enriched in Mo, as shown by the high Mo/Ni surface ratio compared with the nominal one. This finding coincides with the previous conclusion that over this Ni–Mo catalyst, NiO particles are encapsulated within a nickel aluminate shell, reducing the total exposed nickel, whereas molybdate species seem to segregate to the topmost surface layers, possibly coating some of the nickel sites. Vanadium also surface segregates, as indicated by the higher surface versus total V/Ni ratio. These experimental observations coincide with thermodynamic arguments, which demonstrate that surface for most multicomponent systems becomes enriched in the constituent possessing the lowest surface energy. The surface energies of MoO_3 and V_2O_5 are reported to be very low (6 and 9×10^{-6} J/cm^2, respectively) [46]. Although no direct experimental data for NiO are available in the literature, theoretical calculations show that the NiO surface free energy is similar to that of MgO [47], which has been experimentally determined to be 110×10^{-6} J/cm^2 [46]. The surface energies of MoO_3 and V_2O_5 are clearly more than an order of magnitude lower than that predicted for NiO, and thus the Mo and V surface segregation observed over the Ni–Mo and Ni–V catalysts is in line with predictions.

Co, Nb, and Ta metal promoters are less exposed, as reflected by the lower surface Me/Ni ratios, each showing strong surface enrichment by nickel, with the Ni–Nb catalyst exposing the most surface nickel. These interesting results indicate that these particular promoters improve dispersion of the nickel phase, possibly via their intercalation between nickel (oxide) phase and alumina, thus weakening the influence of the underlying support, in accordance with the previous observations, with NiO particles accommodated on

the promoting metal/alumina interface. One may also infer that the surface energies of CoO, Nb_2O_5, and Ta_2O_5 are higher than that of NiO, this providing the thermodynamic driving force for the formation of a nickel oxide capping layer. Unfortunately, there are few reports of experimental surface energies for oxides, and this hypothesis awaits future verification.

3.2. Catalytic performance in ethane ODH reaction and ethene oxidation

The activities of the unpromoted and Me-promoted Ni/Al_2O_3 catalysts were explored under steady-state conditions between 300 and 500 °C, with a constant W/F (0.54 g s/cm^3) and ethane/oxygen (1:1) ratio. Ethane conversion is plotted as a function of temperature in Figs. 6A and 6B. In the series of the unpromoted Ni/Al_2O_3 catalysts (Fig. 6A), increasing Ni loading improved the reactivity. A 50% initial "jump" in conversion occurred when the Ni loading was increased from 8 to 15 wt%, and a further 10% enhancement in activity was found for the 24NiAl catalyst.

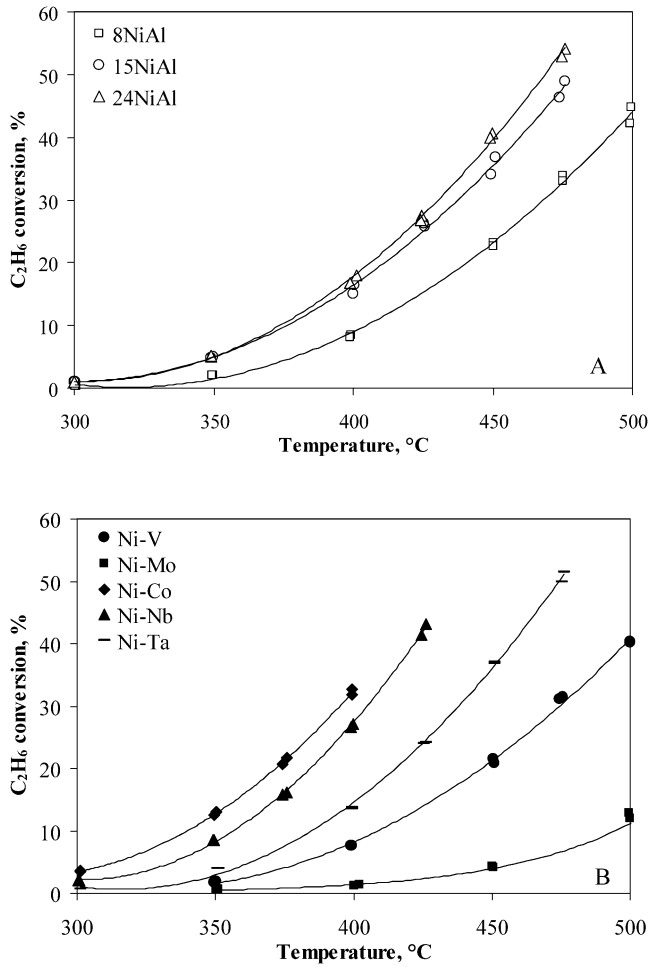

Fig. 6. Ethane conversion as a function of temperature (reaction conditions: $W/F = 0.54$ g s/cm^3, $C_2H_6/O_2 = 1/1$). (A) Unpromoted Ni/Al_2O_3 catalysts; (B) metal promoted Ni/Al_2O_3 catalysts.

Table 4
Ethane conversion at 400 °C and product distribution at constant ethane conversion

	C_2H_6 conversion at 400 °C (%)	Product distribution at 15% C_2H_6 conversion		
		C_2H_4 (%)	CO_2 (%)	CO (%)
8NiAl	8.26	78.95	20.33	0.72
15NiAl	16.44	83.36	16.52	0.12
24NiAl	17.36	79.11	20.64	0.25
Ni–V	7.61	45.96	52.32	1.72
Ni–Mo	1.14	73.25	17.44	9.31
Ni–Co	32.62	43.92	56.07	–
Ni–Nb	27.06	73.22	26.77	–
Ni–Ta	13.70	84.16	15.44	0.4

This nonlinear increase of conversion with loading can be attributed to the presence of large NiO crystals on the surface of 24NiAl, as indicated by the characterization results, for which a significant fraction of the Ni was inaccessible to reactants. However, the formation of crystalline NiO phase did not impair the reaction, since no decline in the conversion was observed, and certainly helps to generate active sites.

The promoted Me–Ni/Al_2O_3 catalysts (Fig. 6B) presented a large variation in the catalytic behavior, depending on the promoting metal, with conversions ranging from 1 to 33% at 400 °C (see Table 4) compared with 18% exhibited by the unpromoted 24NiAl catalyst. The activities of the samples under study decreased in the following order:

$$\text{Ni–Co} > \text{Ni–Nb} > \text{24NiAl} > \text{15NiAl} > \text{Ni–Ta} > \text{8NiAl} = \text{Ni–V} \gg \text{Ni–Mo}.$$

Comparison of the catalysts in terms of specific surface activity ($mol_{C_2H_6}/(m^2\,s)$) does not change the above sequence.

Besides activity, selectivity to the corresponding alkene is also of paramount importance for the evaluation of ODH catalysts. Since selectivity is strongly related to conversion, we conducted a second series of experiments at constant temperature (400 °C), constant ethane/oxygen ratio (1:1), and varying W/F from 0.02 to 1.33 g s/cm^3 in order to attain different conversion levels. Typical product distributions recorded at 15% ethane conversion over the catalysts are tabulated in Table 4. Ethylene selectivity versus ethane conversion is presented in Figs. 7A and 7B. The unpromoted catalysts exhibited high selectivity (80–90%) in the 0–20% conversion range and showed only a slight drop in selectivity for ethylene with increasing conversion due to secondary reactions of the olefin product. A more pronounced decrease was seen for the 8NiAl catalyst, which initially appeared more selective, but finally reached the same limiting selectivity as the 24NiAl for 15% ethane conversion.

The introduction of metal promoters to the Ni–Al system had a great impact on the catalytic performance of the resulting materials in ethane oxidative dehydrogenation. Compared to the 24NiAl catalyst, the incorporation of Co and V induced a major drop in ethylene selectivity to ∼ 50–55%. However, the trend of selectivity versus conversion was different for the two samples, indicating that Ni–Co mainly

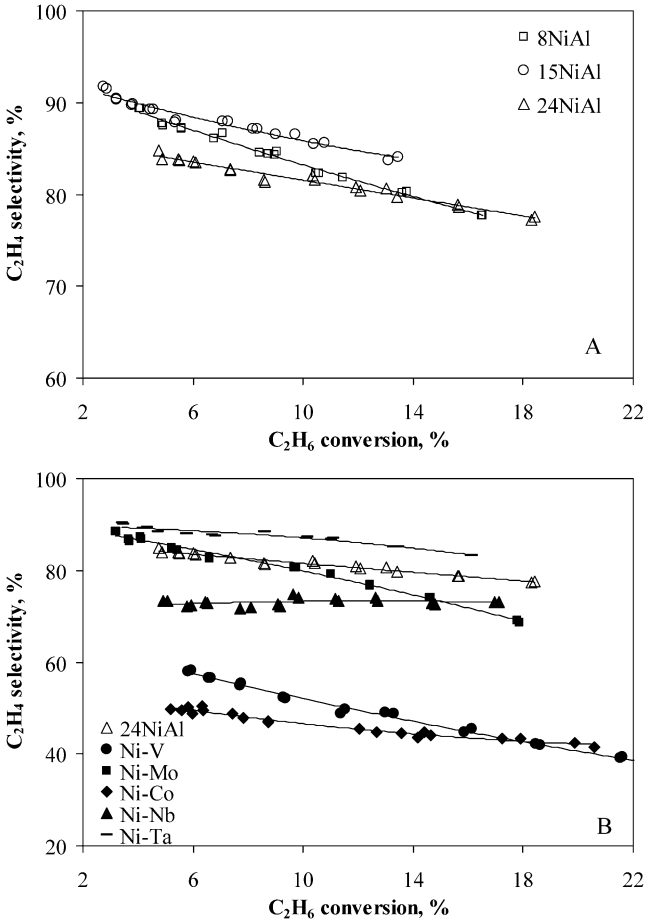

Fig. 7. Ethene selectivity as a function of ethane conversion (reaction conditions: $T = 400\,^{\circ}C$, $C_2H_6/O_2 = 1/1$). (A) Unpromoted Ni/Al_2O_3 catalysts; (B) metal promoted Ni/Al_2O_3 catalysts.

promotes the primary oxidation of ethane to CO_2, whereas over Ni–V both primary and secondary routes of oxidation of ethane and ethylene are enhanced. A similar decrease in selectivity with conversion was also observed for the Ni–Mo catalyst, showing that as in the case of V, early transition metals favor the overoxidation of ethylene. This is also obvious from the product distributions over Ni–V and Ni–Mo catalysts, wherein CO was formed, whereas C_2H_4 and CO_2 were the only carbon-containing reaction products over all of the other samples. Carbon monoxide principally originates from the secondary oxidation of ethene, as demonstrated by our recent studies on MoO_3/Al_2O_3 catalysts [48]. Ni–Mo, on the other hand, does not seem to favor primary ethane oxidation, since it had a very high initial selectivity (90%). Ni–Nb caused a 10% decrease in ethene selectivity (compared with the 24NiAl catalyst), which, however, remained constant with conversion (i.e., there were no secondary reactions). Finally, Ni–Ta proved to be the most effective catalyst in terms of selectivity, being the only catalyst that exhibited a higher selectivity than the 24NiAl sample, which was relatively independent of conversion.

The high ethene selectivities recorded in general over the materials under study imply a low extent of secondary ethene

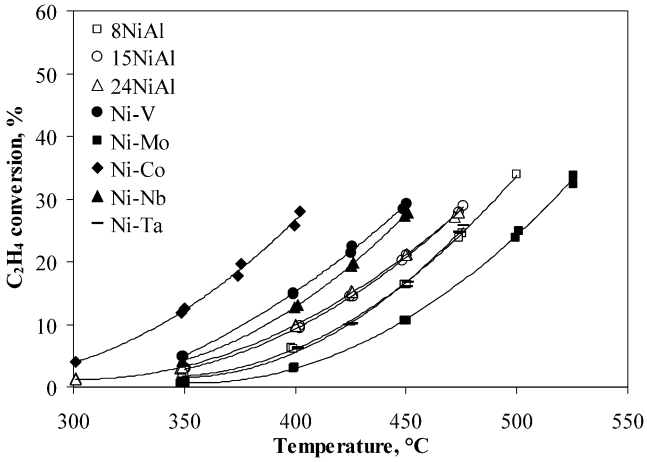

Fig. 8. Ethene conversion as a function of temperature (reaction conditions: $W/F = 0.54\ g\,s/cm^3$, $C_2H_4/O_2 = 1/1$).

oxidation reactions. To study the reactivity of our catalysts toward the olefin product in more detail, complementary experiments were conducted to examine ethene oxidation between 300 and 500 °C. Ethene conversion as a function of temperature is illustrated in Fig. 8. The main product of C_2H_4 oxidation was CO_2, with selectivity for CO ranging under 5%, with the exception of Ni–V and Ni–Mo catalysts, where an average selectivity for CO of 15 and 40%, respectively, was recorded. The relative reactivity of the promoted catalysts toward ethene decreased in the sequence Ni–Co > Ni–V > Ni–Nb > 24NiAl > 15NiAl > Ni–Ta > 8NiAl > Ni–Mo. However, if we compare the ratio of ethylene to ethane consumption rate under identical reaction conditions (reaction temperature, W/F, reaction mixture composition), the sequence changes to the following: Ni–Mo (2.79) > Ni–V (1.95) > Ni–Co (0.95) > 8NiAl (0.74) > 15NiAl (0.58) > 24NiAl (0.55) > Ni–Nb (0.47) > Ni–Ta (0.45).

Only Mo- and V-promoted nickel catalysts exhibit a higher affinity toward ethylene than toward ethane. This clearly presents a serious drawback in the use of these conventional transition metals for light alkane oxidative dehydrogenation, since V and Mo activate ethylene almost twice as efficiently as they do ethane [48]. This also appears to be the case for Ni–Mo and Ni–V catalysts, consistent with their characterization, which reveals the preferential exposure of Mo and V on the surface at the expense of nickel, and the ethane ODH reaction experiments, which show a high extent of secondary reactions on the aforementioned catalysts. Ni–Co is equally reactive toward ethane and ethylene; however, the absence of secondary reactions in ethane ODH, as shown in Fig. 7B, indicates that in the presence of a mixture of alkane and alkene, ethane is preferentially activated. However, it should also be borne in mind that under our working conditions, the partial pressure of ethane in the reaction mixture was much higher than that of ethene, and this may explain this preferential ethane activation. Over all of the other catalysts, reactivity to C_2H_4 is lower, with the Ni–

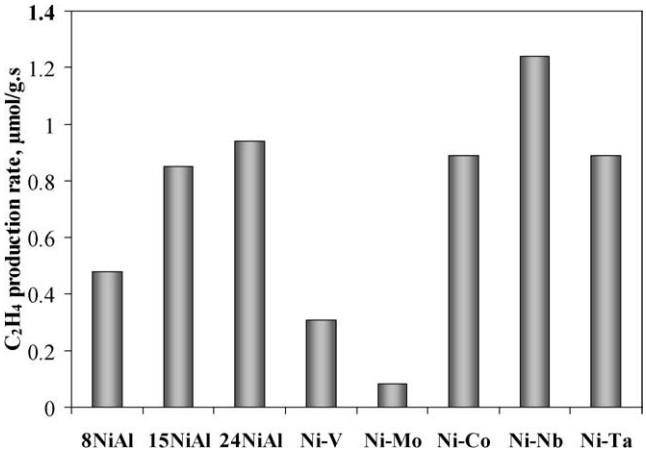

Fig. 9. Ethene production rate at 400 °C (reaction conditions: $W/F = 0.54$ g s/cm^3, $C_2H_6/O_2 = 1/1$).

Nb and Ni–Ta catalysts exhibiting the greatest preference for ethane over ethene activation.

As shown above, the promotion of NiAl catalysts with different metals caused significant changes in the catalytic performance for ethane ODH, with some metals increasing activity but decreasing selectivity for the desired product, etc. To get a clearer picture, ethylene production rates at 400 °C are presented in Fig. 9 for all the samples. It is now apparent that the optimum performance in ethane oxidative dehydrogenation occurs for Ni–Nb, which exhibits the highest rate of ethene production. This is due to the fact that Nb addition caused a great increase in reactivity (over 50% higher conversion) at the expense of a relatively small drop in ethene selectivity. Unfortunately, no direct correlation of the performance of the Ni–Nb catalyst can be made with the data in Symyx patents [17,18]. Compared with NiO/Al_2O_3 catalysts reported in the literature [15,16], our Ni–Nb catalyst exhibits a much improved performance, with over 25% higher ethene productivity.

4. Discussion

The preceding results demonstrate the promise of alumina-supported Ni-based catalysts for the oxidative dehydrogenation of ethane. Nickel, a low-cost metal, appears to be effective in the activation and selective conversion of ethane to ethylene at temperatures below 450 °C, offering ethylene yields much higher than conventional transition metal catalysts used for this reaction. Moreover, the production principally of CO_2 and not CO as the major by-product makes Ni catalysts very attractive from an engineering point of view, since the separation costs downstream from the reactor would be greatly reduced in a potential industrial application of such a process.

The characterization results showed that nickel interacts strongly with alumina, forming a non-stoichiometric surface nickel aluminate phase. At loading higher than 15 wt% Ni, the alumina surface becomes saturated by a two-dimensional $NiAl_2O_4$-like film, and capping islands of NiO particles with increasing size begin to form atop the nickel/alumina interface, as detected by XRD and XPS. In terms of catalytic performance, increasing the Ni loading was beneficial and boosted ethane conversion as a consequence of a rise in the number of active metal-oxide sites, whereas ethylene selectivity levels remained at high levels (∼ 90%), even though larger three-dimensional NiO particles were formed on the catalyst surface. This indicates that both nickel aluminate-like species *and* NiO particles are active and selective. At this point, it should be mentioned that unsupported NiO was also tested in the reaction and exhibited a similar activity per mole of nickel with the 24NiAl catalyst. However, the selectivity for ethylene was very low, with 90% CO_2 production even at low conversion levels. This indicates that free NiO, though active, is unselective, whereas NiO crystallites dispersed on alumina have modified electronic properties, rendering them capable of selectively activating ethane to ethylene but not to CO_2. Even though NiO particles on alumina maintain their crystallographic identity (detected by XRD), the XPS results indicate electronic differences and chemical modification of these NiO particles, indicated by perturbed Ni 2p peak positions for NiO crystallites on 24NiAl compared with that of bulk NiO.

The introduction of promoters (Mo, V, Co, Nb, Ta) in the Ni/Al system induced significant changes in both ethane activity and selectivity for ethene. The most important feature from a structural perspective was the significant nickel surface enrichment, evidenced by XPS, following addition of the second metal. The only exception to this occurred for molybdenum incorporation, wherein Mo preferentially segregates above the nickel/alumina interface, thereby blocking nickel sites. For the rest of the promoting metals, the promoters are accommodated between the alumina support and nickel phase. This reduces the strong metal–support interaction, inhibiting the incorporation of nickel into the alumina lattice, and results in a larger number of exposed Ni reaction sites.

The most positive effect in the performance of nickel catalysts in ethane oxidative dehydrogenation was realized by niobium. The addition of niobium mainly influenced the activation step of the reaction, resulting in an increase in ethane conversion of over 50%, while maintaining a high selectivity for ethene (selectivity fell by only 10% compared with the unpromoted 24NiAl catalyst). Niobium oxide has been reported to enhance metal oxide catalysis in the production of olefins from light alkanes in numerous systems [8,49–53], such as mixed Mo–V–Nb or Mo–V–Te–Nb oxides. It has been postulated that Nb acts as both a structural and electron transfer promoter, enhancing the alkane activation by facilitating the redox cycle of the active metal [53]. If we assume that ethane ODH over Ni-based catalysts proceeds through the classical Mars and van Krevelen redox mechanism occurring over transition metals, then the ease of ethane activation could be related to the ease of the Ni^{2+}/Ni^0 transition, facilitated by the presence of Nb acting as an elec-

tron transfer promoter. The XPS results show that niobium causes a considerable nickel surface enrichment, and the Ni $2p_{3/2}$ BE suggests that Nb weakens the strong interaction between nickel and alumina, with nickel existing in almost pure NiO-like form on the surface of the catalyst. The reducibility studies add additional evidence for a close Ni–Nb interaction, with two reduction processes attributable to Ni–O–Ni and Ni–O–Nb environments. Thus the enhanced activity of the Ni–Nb catalyst in ethane ODH may be related to a highly dispersed pure NiO phase and/or a more facile electron transfer process facilitated by niobium.

5. Conclusions

This study demonstrates that Ni-based alumina-supported catalysts are attractive candidates for the oxidative dehydrogenation of ethane to ethylene, since they exhibit high ethane reactivity at low temperature ($< 450\,^{\circ}C$), low affinity to ethylene oxidation, and very high selectivity for the desired product.

Nickel interacts strongly with alumina, forming surface nickel aluminate-like species in the submonolayer regime, while NiO crystallites form on top of the nickel/alumina interface for multilayer coverages. XPS reveals a chemical modification of the NiO particles on alumina, which possess a bulk-like crystallography but exhibit modified electronic properties that render them selective in ethane ODH; in contrast, unsupported NiO is unselective toward ethene.

Ni promotion with V, Mo, Co, Nb, and Ta significantly modifies both structural and catalytic properties in ethane oxidative dehydrogenation. Promoters were generally intercalated between nickel and alumina, thus reducing the strong nickel–alumina interaction and inhibiting nickel incorporation into the alumina lattice. This enriches the catalyst surface with nickel oxide compared with the undoped catalysts.

The introduction of niobium was the most beneficial for ethane ODH, increasing the reactivity toward ethane by more than 50% while maintaining the high ethene selectivity. It is possible that apart from improving the dispersion of the nickel phase, niobium facilitates the C–H bond activation by acting as an electron transfer promoter.

Acknowledgments

The General Secretariat of Research and Technology (GSRT-PENED01) of Greece and the UK EPSRC under the MIS Network and grant GR/R39436/01 are gratefully acknowledged for financial support of this work.

References

[1] A.H. Tullo, Chem. Eng. News 81 (2003) 21.
[2] E.A. Mamedov, V. Cortes-Corberan, Appl. Catal. A 127 (1995) 1.
[3] T. Blasco, J.M. Lopez Nieto, Appl. Catal. A 157 (1997) 117.
[4] M.A. Banares, Catal. Today 51 (1999) 319.
[5] H.H. Kung, Adv. Catal. 40 (1994) 1.
[6] M.D. Argyle, K. Chen, A.T. Bell, E. Iglesia, J. Phys. Chem. B 106 (2002) 5421.
[7] M.D. Argyle, K. Chen, A.T. Bell, E. Iglesia, J. Catal. 208 (2002) 139.
[8] E.M. Thorsteinson, T.P. Wilson, F.G. Young, P.H. Kasai, J. Catal. 52 (1978) 116.
[9] Y. Liu, P. Cong, R.D. Doolen, S. Guan, V. Markov, L. Woo, S. Zeyß, U. Dingerdissen, Appl. Catal. A 254 (2003) 59.
[10] P. Botella, E. Garcia-Gonzalez, A. Dejoz, J.M. Lopez Nieto, M.I. Vazquez, J. Gonzalez-Calbet, J. Catal. 225 (2004) 428.
[11] J.A. Aderson, L. Daza, D.S. Damyanova, J.L.G. Fierro, M.T. Rodrigo, Appl. Catal. A 113 (1994) 75.
[12] E. Ruckenstein, Y.H. Hu, J. Catal. 162 (1996) 230.
[13] B. Coughlan, M.A. Keane, J. Catal. 138 (1992) 164.
[14] Y. Schuurman, V. Ducarme, T. Chen, W. Li, C. Mirodatos, G.A. Martin, Appl. Catal. A 163 (1997) 227.
[15] X. Zhang, Y. Gong, G. Yu, Y. Xie, J. Mol. Catal. A 180 (2002) 293.
[16] X. Zhang, J. Liu, Y. Jing, Y. Xie, Appl. Catal. A 240 (2003) 143.
[17] Y. Liu, US Patent 6 436 871 (2002), to Symyx Technologies.
[18] Y. Liu, US Patent 6 417 422 (2002), to Symyx Technologies.
[19] I.A.P.S. Murthy, C.S. Swamy, J. Mater. Sci. 28 (1993) 1194.
[20] J. Escobar, J.A. De Los Reyes, T. Viveros, Appl. Catal. A 253 (2003) 151.
[21] M. Wu, D.M. Hercules, J. Phys. Chem. 83 (1979) 2003.
[22] P.K. De Bokx, W.B.A. Wassenberg, J.W. Geus, J. Catal. 104 (1987) 86.
[23] X. Wang, B. Zhao, D. Jiang, Y. Xie, Appl. Catal. A 188 (1999) 201.
[24] M. Lo Jacono, M. Schiavello, A. Cimino, J. Phys. Chem. 75 (1971) 1044.
[25] F.M.T. Mendes, C.A. Perez, R.R. Soares, F.B. Noronha, M. Schmal, Catal. Today 78 (2003) 449.
[26] I.E. Wachs, Y. Chen, J. Jehng, L.E. Briand, T. Tanaka, Catal. Today 78 (2003) 13.
[27] M. Atanasov, D. Reiner, J. Electron Spectrosc. Relat. Phenom. 86 (1997) 185.
[28] J. Wang, L. Dong, Y. Hu, G. Zheng, Z. Hu, Y. Chen, J. Solid State Chem. 157 (2001) 274.
[29] M. Jitianu, A. Jitianu, M. Zaharescu, D. Crisan, R. Marchidan, Vibr. Spectrosc. 22 (2000) 75.
[30] J.P. Espinos, A.R. Gonzalezelipe, A. Fernandez, G. Munuera, Surf. Interface Anal. 19 (1992) 508.
[31] M.M. Natile, A. Glisenti, Chem. Mater. 14 (2002) 4895.
[32] M.J. Tomellini, J. Chem. Soc., Faraday Trans. 1 84 (1988) 3501.
[33] M.W. Roberts, R.J. Smart, J. Chem. Soc., Faraday Trans. 1 80 (1984) 2957.
[34] P. Salagre, J.L.G. Fierro, F. Medina, J.E. Sueiras, J. Mol. Catal. A 106 (1996) 125.
[35] S. Uhlenbrock, C. Scharfschwerdt, M. Neumann, G. Illing, H.J. Freund, J. Phys. Condens. Matter 4 (1992) 7973.
[36] M.A. van Veenendaal, G.A. Sawatzky, Phys. Rev. Lett. 70 (1993) 2459.
[37] P. Dufresne, E. Payen, J. Grimblot, J.P. Bonnelle, J. Phys. Chem. 85 (1981) 2344.
[38] J.C. Vedrine, G. Hollinger, T.M. Duc, J. Phys. Chem. 82 (1978) 1515.
[39] S. Kasztelan, J. Grimblot, J.P. Bonnelle, E. Payen, H. Toulhoat, Y. Jacquin, Appl. Catal. 7 (1983) 91.
[40] E. Heracleous, A.F. Lee, I.A. Vasalos, A.A. Lemonidou, Catal. Lett. 88 (2003) 47.
[41] S.R.J. Carrazan, C. Peres, J.P. Bernard, M. Ruwet, P. Ruiz, B. Delmon, J. Catal. 158 (1996) 452.
[42] B.P. Barbero, L.E. Cadús, L. Hilaire, Appl. Catal. A 246 (2003) 237.
[43] G.E. McGuire, G.K. Schweitzer, T.A. Carlson, Inorg. Chem. 12 (1973) 2450.
[44] L. Dragone, P. Moggi, Appl. Surf. Sci. 187 (2002) 82.

[45] M.M. Natile, A. Glisenti, Chem. Mater. 14 (2002) 3090.
[46] S.H. Overbury, P.A. Bertrand, G.A. Somorjai, Chem. Rev. 75 (1975) 547.
[47] M.B. Taylor, C.E. Sims, G.D. Barrera, N.L. Allan, W.C. Mackrodt, Phys. Rev. B 59 (1999) 6742.
[48] E. Heracleous, A.A. Lemonidou, Appl. Catal. A 264 (2004) 73.
[49] H.M. Swaan, Y. Li, K. Seshan, J.G. Van Ommen, J.R.H. Ross, Catal. Today 16 (1993) 537.
[50] J.C. Védrine, G. Coudurier, A. Ouqour, P.G. Pries de Oliveira, J.C. Volta, Catal. Today 28 (1996) 3.
[51] P. Viparelli, P. Ciambelli, L. Lisi, G. Ruoppolo, G. Russo, J.C. Volta, Appl. Catal. A 184 (1999) 291.
[52] F. Barbieri, D. Cauzzi, F. De Smet, M. Devillers, P. Moggi, G. Predieri, P. Ruiz, Catal. Today 61 (2000) 353.
[53] B. Kilos, M. Aouine, I. Nowak, M. Ziolek, J.C. Volta, J. Catal. 224 (2004) 314.